Measuring a 5G Millimeter-Wave Device's Spherical Coverage

Brett T. Walkenhorst
NSI-MI Technologies
Suwanee, GA 30024
bwalkenhorst@nsi-mi.com

Prasadh Ramachandran
Keysight Technologies
Oulu, Finland
prasadh.ramachandran@keysight.com

***Abstract*— A new over-the-air (OTA) metric called "spherical coverage" is being discussed in 3GPP. The concept is to test the ability of a device to reliably form beams in any direction, offering connectivity in any orientation and polarization. In this paper, we analyze the effectiveness of various test environments for testing spherical coverage at millimeter-wave frequencies for 5G devices.**

***Index Terms*—5G, far-field, compact range, millimeter-wave**

I. Introduction

With the proposed use of millimeter-wave frequency bands for the 5G enhanced mobile broadband (eMBB) use case, the telecom industry faces several new challenges. To mitigate the high propagation loss, beamforming antennas are used at both the user equipment (UE) and the next generation Node B (gNB), which is 5G's version of a base station system. In developing systems for deployment, vendors are using phased arrays to implement the required beamforming.

Phased arrays have a fundamental limitation in terms of the scan angles that they can cover while meeting their gain requirements [1]. In addition, a typical mobile UE's orientation is not fixed with respect to the gNB, which can create coverage issues if there is no beam from the UE pointing toward the gNB and/or its surrounding scattering clusters. This has driven the need to have multiple antenna modules on a UE to cover different spatial directions so the UE has connectivity at all possible angles regardless of its orientation or position.

To address the testability of this spatial coupling requirement, 3GPP is defining a new metric called "spherical coverage". The intent is to quantify the UE's capability to have a uniform performance irrespective of the orientation of the UE with respect to the gNB. This paper looks at the impact of measuring a UE's spherical coverage in various test environments and examines the errors introduced under various assumptions.

To achieve this objective, we first look at the details of spherical coverage testing in Section II. In Section III, we describe two different test environments to be assessed. To examine the effect of each environment on the test metric, we set up a simulation with an antenna model described in Section IV and a detailed description of the simulation methodology in Section V. Results are described in Section VI followed by conclusions in Section VII.

II. Spherical Coverage Testing

Spherical coverage testing is being defined for both EIRP and EIS measurements. A conformance test for a UE begins with a gNB emulator establishing a call. This keeps the UE in a connected mode as if it were in a live network.

Using a two-axis positioner, the UE is then rotated to various angles around a sphere with a certain angular step size, either fixed or variable. The details of the sampling scheme are still being finalized by 3GPP [2]. At each angle, the UE is allowed some dwell time to select its ideal subarray and beam state after which the test equipment measures EIRP in the traditional way [2].

The ensemble of EIRP values thus measured around the sphere is used to compute an empirical cumulative distribution function (CDF). Using this CDF, we can estimate how well the device will function at various probability levels. 3GPP is still finalizing the details of those performance requirements.

The procedure for EIS spherical coverage is identical except that the direction of the link is swapped and EIS is computed at each position instead of EIRP.

III. Test Environments

Of the test environments being considered in 3GPP, the two that offer the most likely solution for spherical coverage are the quasi-far-field chamber and the compact range. Each of these test environments is described briefly here.

A. Quasi-far-field chamber

In [2], a test method is described called Direct Far-Field (DFF). This is essentially a far-field chamber where the range length is computed based on the size of the radiating portion of the aperture, not the size of the device under test (DUT). Because this method does not strictly obey the traditional far-field constraint, we call it quasi-far-field (QFF). If we assume, for example, that the active subarray is no larger than 5 cm, then at 43.5 GHz, a range length of 72.5 cm is sufficient to ensure the subarray experiences no more than 22.5 deg of phase taper when the center of the subarray is aligned with the range axis. This is the basic assumption employed in the DFF test environment under "DUT Antenna Configuration 1" in [2], the simplest specified model for a DUT. DUT sizes up to 15 cm are expected to be tested in this environment under the assumption that any phase-coherent subarrays are limited to 5 cm in extent or less.

In order to achieve a sufficient signal-to-noise ratio (SNR), it is expected that the QFF system will employ a probe with a gain of approximately 20 dBi. We assume the probe response may be approximated by a circularly symmetric Gaussian beam. We compute the magnitude response as a function of polar angle by

$$|E(\theta)| = e^{kb(\cos\theta - 1)} \frac{1 + \cos\theta}{2} \quad (1)$$

where the value of b is found by numerically inverting

$$D = \frac{4}{\frac{1}{kb} - \frac{1}{2(kb)^2} + \frac{1}{8(kb)^3}(1 - e^{-4kb})} \quad (2)$$

for a given directivity value D.

A derivation of the above equations is found in the Appendix.

B. Compact range

Another test method in [2], called Indirect Far-Field (IFF) employs the use of a reflector and is more commonly called a compact antenna test range (CATR) or compact range. Two compact range reflectors were designed and simulated for this study. One was designed for a 15 cm quiet zone (QZ) where the 15 cm UE device is completely enclosed by the cylindrical QZ. Another was designed for a 50 cm QZ as an alternative, oversized system. This design was manufactured, and field probe data was collected to validate the model.

Both reflectors used rolled-edge treatment and were simulated using the Blended Rolled-Edge Compact Range Reflector Code (BRCRRC) [3]-[4].

IV. Antenna Model

The antenna under test (AUT) is expected to be a phased array antenna, capable of beam steering to some finite angular resolution. To model the phased array on the AUT, we employ arrays of point sources. Each of these sources sets up a field at observation point $\vec{r}$ given by

$$\vec{E}_m(\vec{r}) = w_m \frac{e^{-jk\|\vec{r}-\vec{r}_m'\|}}{\|\vec{r}-\vec{r}_m'\|}\hat{e}_1 \quad (3)$$

where w_m is a complex weight associated with the m^{th} source, k is the wave number, $\vec{r}_m'$ is the position of the source, and $\hat{e}_1$ is the polarization orientation. The direction of $\hat{e}_1$ is arbitrary, but using a dual-polarized probe as specified in [2], the polarization of the AUT can be matched by the measurement system. We therefore only consider the co-polarized component in our analysis.

We model the AUT's antenna arrays as a rectangular grid of Nx2 elements. Targeting approximately 15 or 45 degree beamwidths, the inter-element spacings of 0.5λ, 1.0λ, and 0.6λ were chosen for N = 8, 4, and 2, respectively.

For UEs, we assume that beamforming is achieved with simple phase shifters with low-cost digital-to-analog converters (DACs) on the control lines. If we assume the DACs have 4 bits of control, we have a minimum step size of 22.5 degrees on the individual phase shifters. At boresight, this gives us approximately 7.2, 3.6, and 6.0 deg of resolution for each of the AUT models, respectively. If we assume a 2-bit DAC on each phase shifter, we have 30, 14.5, and 24.6 deg resolution near boresight. To simplify the beam steering model, we analyze fixed angular resolutions of 3, 6, 10, and 20 deg spanning +/-60 deg in azimuth and elevation.

The placement and orientation of the arrays within the device are variable. Figure 1 shows an 8x2 array oriented vertically, placed at the left-most position while still maintaining a maximum extent of 15 cm for the device.

Figure 2 shows the 2-dimensional far-field response of the broadside-steered beam of the 8x2 array shown in Figure 1.

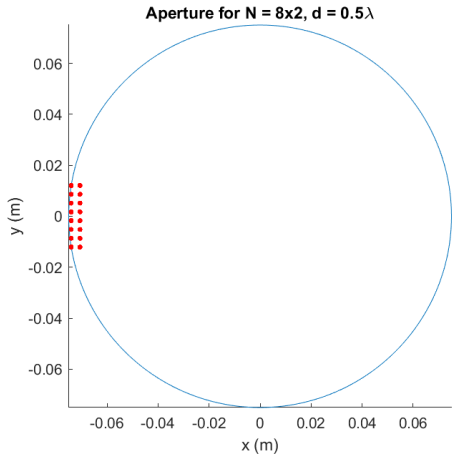

Figure 1. Example of 8x2 subarray configuration

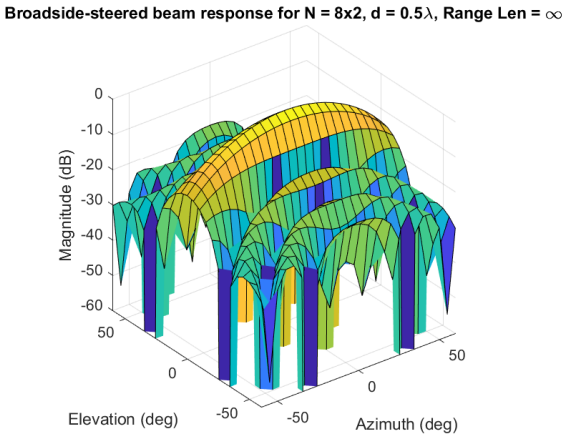

Figure 2. Broadside beam response of 8x2 subarray

V. Simulation Description

A. Quasi-far-field chamber

For the far-field simulation, the measurement probe is modeled as a point source that excites fields similar to (3); but using reciprocity, the source and observation vectors are swapped and the complex weights of the array elements are dropped. We write these fields as

$$\vec{E}_m(\vec{r}) = \frac{e^{-jk\|\vec{r}_m + L\hat{z}\|}}{\|\vec{r}_m + L\hat{z}\|}\hat{e}_1 \quad (4)$$

where we have set $\vec{r}' = -L\hat{z}$ where L is the range length, and we have set the origin of the coordinate system to be at the center of our 15 cm DUT.

The fields are computed at positions defined by the locations of the point sources comprising the subarray. We then rotate the aperture in azimuth and elevation in 5 deg steps over +/- 60 deg and apply a different set of complex weights, w_m, to achieve different beam states.

As described above, we assume alignment of the probe's polarization vector with that of the subarray. The complex voltage received by the array, for each AUT orientation and each beam state, is computed as

$$V = \sum_m w_m\left(\vec{E}_m(\vec{r}) \cdot \hat{e}_1\right) = \sum_m w_m \frac{e^{-jk\|\vec{r}_m - \vec{r}'\|}}{\|\vec{r}_m - \vec{r}'\|} \quad (5)$$

We normalize the voltage by L to enable us to compare results across multiple range lengths, i.e.

$$\bar{V} = LV = \sum_m w_m L \frac{e^{-jk\|\vec{r}_m - \vec{r}'\|}}{\|\vec{r}_m - \vec{r}'\|} \quad (6)$$

B. *Compact range*

Fields in the compact range are computed using the BRCRRC simulation code, as mentioned previously. The fields were computed in a volume with a spacing of λ. A denser grid of points proved prohibitive to simulate, but a spectral analysis showed that the resolution of λ yielded an oversampled condition, which allowed us to use the simulated data as an interpolant.

As an approximation to the normalization that would occur with a standard gain horn mounted in the center of the QZ for calibration, we normalize the fields in the QZ such that the centerline cut along the z-axis has an average power of one.

For each AUT model and each AUT orientation, fields were computed by interpolating the complex fields of the QZ volume to the positions defined by the point sources comprising the AUT subarray over all orientation angles. Beam steering weights were then applied and complex voltages computed using

$$V = \sum_m w_m \left(\vec{E}_m(\vec{r}) \cdot \hat{e}_1\right) \quad (7)$$

where $\vec{E}_m(\vec{r})$ are the fields obtained by cubic interpolation.

For the 50 cm CATR that was manufactured, we obtained samples of the QZ using a standard gain horn (SGH) mounted on a three-axis positioner. Due to logistical constraints, we were only able to sample a depth of 9 cm, so we restrict our analysis of AUT orientation angles to +/- 20 deg to ensure the AUT stays within the sampled volume of the QZ.

Approximating the SGH as a point source, we treat the received voltages as fields and use the same method of interpolation and computation of voltages as described above.

In Figure 3, we show a rendering of the compact range that was measured.

Figure 3. Rendering of manufactured 50 cm CATR

VI. Simulation Results

While a number of configurations were simulated, the results shown here correspond to the configuration of the 8x2 array with beam steering resolution of 6 degrees at 43.5 GHz. This configuration most clearly illustrates the issues with the different test environments. Coarser beam steering resolutions show similar trends, but are more difficult to interpret due to fewer data points. Lower frequencies exhibit less error than higher frequencies in both test environments.

After complex voltages for all beam states and all AUT orientations are computed, we compute the magnitude of the voltages and, assuming the AUT always makes the ideal choice of beam state for any given orientation, we take the maximum value over all beam states for each AUT orientation.

From these values, we compute an empirical CDF and the values of the CDF at various probability levels are computed as metrics. We can then compare these metrics across different test environments and compute any deviation from the ideal case of perfect plane-wave illumination.

For QFF, we simulated range lengths of 72.5 cm (the far-field (FF) distance at 43.5 GHz assuming a 5 cm aperture), 1 m, 2 m, and 6.525 m (the FF distance at 43.5 GHz for the 15 cm aperture).

For the CATR, we simulated both 15 cm and 50 cm QZ systems as well as the measured data for the 50 cm QZ system.

The ideal case of a perfect plane wave illuminating the aperture is used as the baseline. It is computed using a modified form of the QFF field computation

$$\vec{E}_m(\vec{r}) = e^{-jk(\vec{r}_m \cdot \hat{z})} \hat{e}_1 \quad (8)$$

where we only consider the z-component of the location of the point sources as would be the case with a plane wave emanating from infinitely far away in the negative z-direction.

The empirical CDFs of the EIRP for the QFF system at various range lengths are shown in Figure 4 along with the CDF of the ideal plane-wave condition.

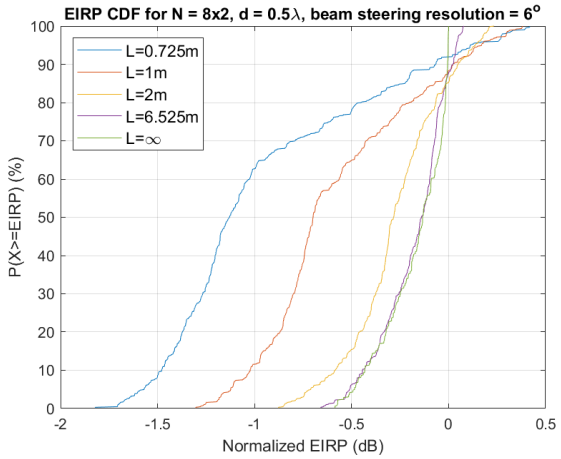

Figure 4. CDFs of QFF and ideal plane wave (L=∞)

The empirical CDFs of the EIRP for the two simulated CATRs are shown in Figure 5 along with the CDF of the ideal plane-wave condition.

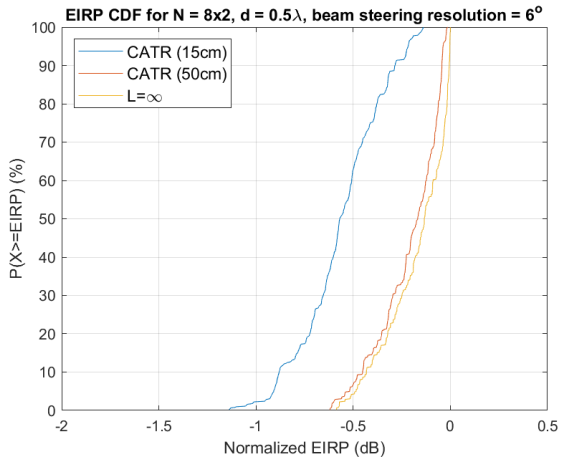

Figure 5. CDFs of simulated CATRs and ideal plane wave (L=∞)

Considering that the difference between the QFF and CATR CDFs and the ideal plane-wave CDF at each probability level constitute an error for each test method, we plot that difference in Figure 6 and Figure 7 below for QFF and CATR, respectively. Note that the plane-wave curve is plotted, but is zero everywhere, so it appears as a vertical line.

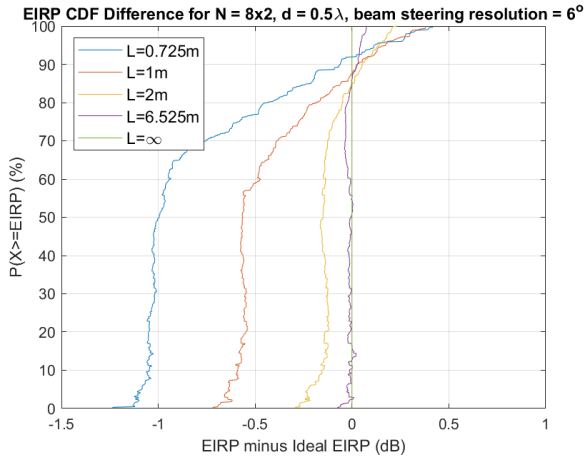

Figure 6. CDFs of QFF minus ideal plane wave (L=∞)

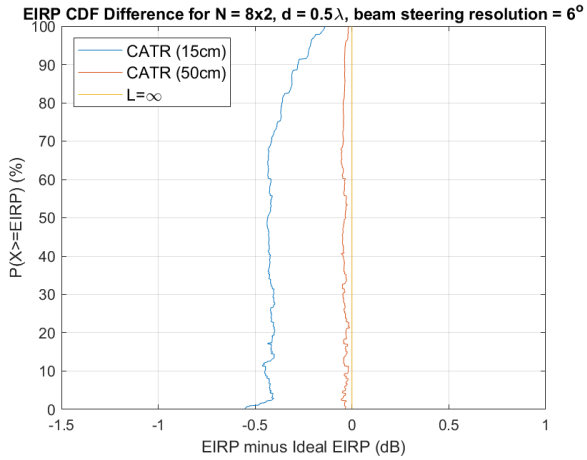

Figure 7. CDFs of simulated CATRs minus ideal plane wave (L=∞)

Figure 8 shows the difference between the empirical CDF for the measured QZ data on the manufactured 50 cm CATR with that of the ideal plane wave.

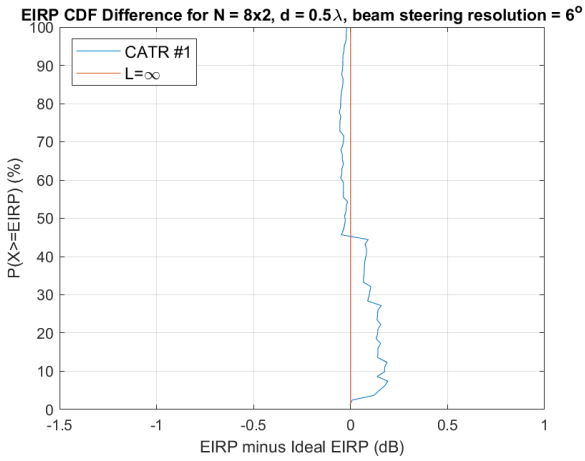

Figure 8. CDFs of measured 50 cm CATR and ideal plane wave (L=∞)

Compare the results of Figure 8 to the red curve, labeled "CATR (50cm)", in Figure 7. The overall deviation of the results is similar, though a bit larger in Figure 8. This is likely due to effects not modeled by our simulation tool. Two of these effects are deviations of the reflector surface from ideal and scattering from other sources within the chamber. The increased ripple due to these effects causes the calibration point in the center of the QZ to give us a normalization that leads to both positive and negative errors where the simulated results gave only negative errors.

A. Discussion of Results

There are two main drivers for the error seen in the QFF system (Figure 6).

The first driver deals with variations in the link distance. Any offset of the aperture from the center of rotation will cause the aperture to move toward and away from the measurement probe as the AUT is rotated. The magnitude variation due to that motion is exacerbated by short range lengths.

The second driver is due to the probe directivity. For short range lengths, the angular extent of the AUT from the perspective of the probe gets larger. This leads to a larger rolloff in the probe response. For our AUT shown in Figure 1, the combination of these two effects causes a variation in the beam responses as a function of azimuth angle. The ideal FF condition should lead to a peak beam response that is relatively flat across azimuth. In contrast, Figure 9 shows the azimuth cross-section of all beam patterns for the shortest range length of L = 0.725m.

The main driver of the error in the CATR (Figure 7) is the taper of the feed pattern at the edge of the QZ. This has the effect of reducing the amplitude at the edge relative to the center of the QZ where our calibration measurement is made.

All these effects, for both QFF and CATR, could be mitigated by placing the aperture in the center of the QZ, but one of the key assumptions for UE testing in 3GPP is that the DUT is effectively a black box to its tester. Details of the antenna locations and configurations are not expected to be provided by the manufacturer. Even if we had that information, as we rotate the DUT, the active subarray will almost certainly have to change at some point to ensure full spherical coverage. Since those antenna subarrays can be located anywhere on the device, we can't mount all possible subarrays in the center of the QZ simultaneously.

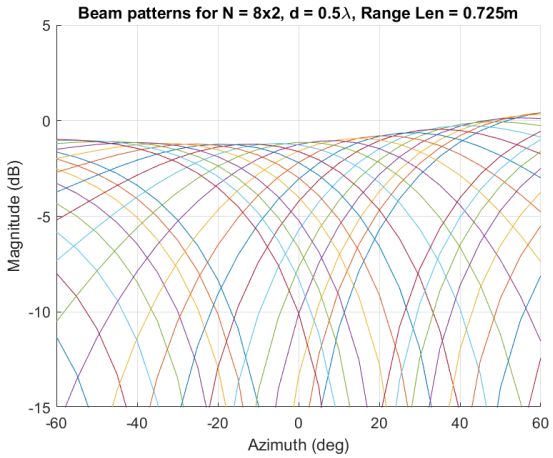

Figure 9. QFF beam patterns vs azimuth, L = 0.725m

B. *Summary*

Another view of the results may be obtained by picking off error values at various probability levels. For outage, it probably makes sense to select low probability levels. To get a sense of what happens at the median, we can look at 50%. And to see where we are on estimating near the peak SNR levels, we might look at high probability levels. In 3GPP, various probability levels have been discussed including the values we have chosen.

In Table 1, we show a summary of error levels at 10%, 20%, 50%, 80%, and 90% probability levels for the various test environments we have analyzed.

Table 1. Summary of Spherical Coverage Errors

	Standard Size Chambers		Oversized Chambers	
	QFF (L=72.5 cm)	CATR (D=15 cm)	QFF (L=6.25m)	CATR (D=50 cm)
P = 10%	-1.05 dB	-0.45 dB	-0.01 dB	-0.02 dB
P = 20%	-1.05 dB	-0.40 dB	-0.01 dB	-0.03 dB
P = 50%	-1.00 dB	-0.43 dB	-0.01 dB	-0.03 dB
P = 80%	-0.43 dB	-0.36 dB	-0.02 dB	-0.05 dB
P = 90%	-0.06 dB	-0.28 dB	0.02 dB	-0.04 dB

VII. Conclusion

In this paper, we have analyzed errors resulting from the use of two types of chambers to make UE measurements for ascertaining spherical coverage. Errors on the order of 0.5 to 1.0 dB for various probability levels of interest are estimated for the default test configurations.

For the default configurations, the compact range gives us a significantly lower error than the QFF chamber. However, at the expense of a larger chamber, far-field chambers with larger probe-to-AUT separation and CATRs with oversized QZs may be used to reduce the errors of both types of systems.

Appendix

Here, we derive the equations for computing the pattern of a circularly symmetric Gaussian beam of a given directivity.

From [5], we write the field resulting from a Gaussian feed pattern as

$$E(r,\theta,\phi) = N_f \frac{e^{-jkr}}{kr} e^{kb\cos\theta}(1+\cos\theta)\left(\cos\phi\,\hat{\theta} - \sin\phi\,\hat{\phi}\right) \quad (9)$$

where N_f is a normalization constant, k is the wave number, and b is a factor dictating the width of the beam.

The magnitude of the co-pol field strength is given by

$$|E(r,\theta)| = \frac{N_f}{kr} e^{kb\cos\theta}(1+\cos\theta) \quad (10)$$

To normalize the peak response to 0 dB, we set

$$N_f = \frac{kr}{2e^{kb}} \quad (11)$$

leading to

$$|E(\theta)| = e^{kb(\cos\theta-1)}\frac{1+\cos\theta}{2} \quad (12)$$

In general, directivity is written as

$$D = \frac{4\pi}{\int_0^{\pi} d\theta \int_0^{2\pi} d\phi |E(\theta,\phi)|^2 \sin\theta} \quad (13)$$

but since $|E(\theta)|$ is circularly symmetric, we can write

$$D = \frac{2}{\int_0^{\pi} |E(\theta)|^2 \sin\theta\, d\theta} \quad (14)$$

Substituting the equation for $|E(\theta)|$ above, we find

$$D = \frac{2}{\int_0^{\pi} e^{2kb(\cos\theta-1)} \frac{(1+\cos\theta)^2}{4} \sin\theta\, d\theta} \quad (15)$$

The integration is fairly tedious, but ultimately leads to

$$D = \frac{4}{\frac{1}{kb} - \frac{1}{2(kb)^2} + \frac{1}{8(kb)^3}(1-e^{-4kb})} \quad (16)$$

We can numerically invert the equation above to solve for b, then use that value to solve for the angular response of the Gaussian beam pattern using (12).

Acknowledgment

The authors gratefully acknowledge the work of Vivek Sanandiya for his support in collecting volumetric field probe data in the 50 cm CATR.

References

[1] C.A. Balanis, *Antenna theory: analysis and design*. John Wiley & Sons, 2016.

[2] 3GPP TR 38.810 V2.6.0, "Study on test methods for New Radio," Sep 2018

[3] Gupta, I.J. and Burnside, W.D., "User Manual for Blended Rolled Edge Compact Range Reflector Code (BRCRRC)," *OSU-ESL Technical Report 721929-3*, Jul 1989

[4] Gupta, Inder J., Ericksen, Kurt P., and Burnside, Walter D., "A Method to Design Blended Rolled Edges for Compact Range Reflectors," *IEEE Trans Antennas Propagation.*, Vol AP-38, No. 6, pp. 853-861, Jun 1990

[5] K. Pontoppidan, "Technical description of GRASP8," *TICRA*, p. 106, Feb 2003